Three-dimensional self-consistent radiation transport model for the fluid simulation of plasma display panel cell

H. C. Kim, S. S. Yang, and J. K. Lee[a)]
Department of Electronic and Electrical Engineering Pohang University of Science and Technology, Pohang 790-784, South Korea

(Received 11 February 2003; accepted 1 April 2003)

In plasma display panels (PDPs), the resonance radiation trapping is one of the important processes. In order to incorporate this effect in a PDP cell, a three-dimensional radiation transport model is self-consistently coupled with a fluid simulation. This model is compared with the conventional trapping factor method in gas mixtures of neon and xenon. It shows the differences in the time evolutions of spatial profile and the total number of resonant excited states, especially in the afterglow. The generation rates of UV light are also compared for the two methods. The visible photon flux reaching the output window from the phosphor layers as well as the total UV photon flux arriving at the phosphor layer from the plasma region are calculated for resonant and nonresonant excited species. From these calculations, the time-averaged spatial profiles of the UV flux on the phosphor layers and the visible photon flux through the output window are obtained. Finally, the diagram of the energy efficiency and the contribution of each UV light are shown. [DOI: 10.1063/1.1577399]

I. INTRODUCTION

In plasma devices used as light sources, such as fluorescent lamps, dielectric barrier discharges, and excimer lasers, atoms excited from a ground state by electron-impact collisions radiate photons. Nonresonant photons escape the system very rapidly without being trapped. However, resonant photons suffer many absorptions and re-emissions by the ground state atoms before they escape the system. This phenomenon is called resonance radiation trapping. It makes the apparent radiative decay time much longer than the vacuum radiative decay time, and leads to a significant change of emission spectra. Thus, resonance radiation trapping plays an important role in the performance of light sources.[1]

Plasma display panels (PDPs) use UV photons from the microdischarges for generating the light of display. It is one of the most promising technologies for large area flat displays and wall-hanging high-definition color television.[2,3] However, there remain important issues to be solved, such as improvement of luminous efficiency, reduction of power consumption, and increment of the lifetime.[4] Optimizing the properties of PDP can be aided by understanding the microdischarge physics inside a PDP cell.

The light emission of a PDP cell is based on high-pressure glow discharge whose typical dimensions are in a few hundred μm range and which forms the basic picture element of the display. Plasma display panels use UV photons that are converted into visible photons by red, green, and blue phosphors. The UV photons are generated from the discharge of a neon, helium, and xenon gas mixture. The dominant UV emissions in the PDPs are the 147-nm light from the $Xe^*(^3P_1)$ resonant excited state, the 173-nm light from $Xe_2^*(^3\Sigma_u^+)$ or $Xe_2^*(^1\Sigma_u^+)$ excimers, and the 150-nm light from $Xe_2^*(O_u^+)$ excimer.

Although direct experimental access is difficult due to the small system size of a PDP cell, the discharge diagnostics by optical measurements have been performed over the last few years, such as spatiotemporal behaviors of excited xenon atoms by using optical emission and laser absorption techniques,[5–7] electric field by using the laser-induced fluorescence technique,[8] and electron density and temperature by using the laser Thomson scattering method.[9] Numerical simulation is also a useful tool to provide detailed information on the microdischarge characteristics in a PDP cell. There have been many numerical models of PDP discharges over the last few years.[10–18] One-dimensional models are sufficient for simulating matrix-type PDP,[10–12] while the study of coplanar-type PDP requires at least two-dimensional (2D) modeling.[13–15] The three-dimensional (3D) variations of the cell structure require 3D models.[16–18]

In most of numerical models of PDP discharges, the concept of an escape factor (inverse of trapping factor) has been used for an approximate formulation of incorporating trapping effects. The strict kinetics of resonant photons is described by using a multiple-scattering representation[19,20] or solving the Holstein equation mathematically.[21] Since the trapping factor approach (TFA) assumes constant effective decay time, it is valid only when the spatial distribution of resonant excited species is uniform or identical to the lowest-order eigenmode solution of Holstein equation, and the spatial redistribution of resonant excited species cannot be considered.

For the multiple-scattering representation, Monte Carlo simulation is used to solve the probabilities that a photon escapes after suffering absorption and re-emission processes.[22–24] It is a general and wholly numerical algo-

a)Electronic mail: jkl@postech.ac.kr

rithm for the modeling of complex physical processes. However, it is not self-consistently coupled to a fluid model because of its high computational cost. For the self-consistent model, the Holstein equation should be solved mathematically. Recently, Lee *et al.*[25] have developed a 2D radiation transport (RT) model coupled with a fluid simulation using the propagator function method (PFM).[26] This method has been also applied to a particle simulation in capacitively coupled discharges and inductively coupled discharges as well as a fluid simulation in PDP discharges.[27–29]

In this article, we report on the 3D RT model coupled with the 3D fluid simulation,[17] using the PFM to incorporate the resonance radiation trapping properly as a generalization of the 2D RT model of Ref. 25. The mathematical description of the 3D Cartesian RT model is presented in Sec. II. Section III shows the results calculated by using the model of Sec. II as well as the comparison with the TFA. Finally, our works are summarized and discussed in Sec. IV.

II. DESCRIPTION OF THE MODEL

For this study, we have used a 3D fluid code (FL3P) for a PDP cell which has been published previously.[17,30,31] It has been modified to include more species such as dimer ions and their related chemical reactions. In particular, $NeXe^+$ significantly affects the distribution of the excited species. This code is based on the solution of transport equations (continuity and momentum transfer using a drift-diffusion approximation) for electrons, ions [Xe^+, Xe_2^+, Ne^+, Ne_2^+, $NeXe^+$], and excited species [$Xe^*(^3P_1)$,$Xe^*(^3P_2)$, $Xe_2^*(O_u^+)$, $Xe_2^*(^1\Sigma_u^+)$, $Xe_2^*(^3\Sigma_u^+)$, Xe**, Ne*, and Ne**] along with Poisson's equation for the electric potential. Xe** and Ne** stand for the sum of $6s'$, $6p$, $5d$, $7s$ states of xenon and $3p$ states of neon (Racah notations), respectively. The emission spectra of 147, 150, 173, and 828 nm from the xenon excited species and 600 nm from the neon excited species are also included. The schematic diagram of a coplanar ac PDP is shown in Fig. 1 of Ref. 17.

Beginning with the modified Holstein equation for the excited species, we derive the 3D RT model as a generalization of model presented in Ref. 25 in two dimensions:

$$\frac{\partial n^*(\mathbf{r},t)}{\partial t}+\nabla\cdot\mathbf{\Gamma}(\mathbf{r},t)=S(\mathbf{r},t)+\frac{1}{\tau_v}\int n^*(\mathbf{r}',t)G(\mathbf{r},\mathbf{r}')d\mathbf{r}', \quad (1)$$

where $n^*(\mathbf{r},t)$, $\mathbf{\Gamma}(\mathbf{r},t)$, and $S(\mathbf{r},t)$ are the number density, the particle flux, and the source term for the excited species, respectively. τ_v is the vacuum radiative decay time, which is 3.56 ns for the $Xe^*(^3P_1)$ state. The source term $S(\mathbf{r},t)$ includes the loss term of the excited species density due to vacuum radiative decay defined as

$$S^r(\mathbf{r},t)=-n^*(\mathbf{r},t)/\tau_v. \quad (2)$$

$G(\mathbf{r},\mathbf{r}')$ is the kernel function, which is the probability for a photon emitted at the position $\mathbf{r}'$ to be reabsorbed at the position $\mathbf{r}$.

When a photon emitted at the position $\mathbf{r}'$ is reabsorbed at the position $\mathbf{r}$ and the re-emission of the photon is assumed to be isotropic, the kernel function is calculated from the transmission factor $T(\mathbf{r},\mathbf{r}')$:

$$G(\mathbf{r},\mathbf{r}')=-\frac{\mathbf{R}}{4\pi R^3}\cdot\nabla_{\mathbf{r}}T(\mathbf{r},\mathbf{r}')=-\nabla_{\mathbf{r}}\cdot\left[\frac{\mathbf{R}}{4\pi R^3}T(\mathbf{r},\mathbf{r}')\right]+\delta(\mathbf{r},\mathbf{r}'), \quad (3)$$

where $\mathbf{R}=\mathbf{r}-\mathbf{r}'$ and $R=|\mathbf{R}|$. The transmission factor is defined as

$$T(\mathbf{r},\mathbf{r}')=\int_0^\infty g(\nu,\mathbf{r}')\exp\left[-\int_{\mathbf{r}'}^{\mathbf{r}}k(\nu,\mathbf{s})ds\right]d\nu, \quad (4)$$

where $g(\nu,\mathbf{r}')$ and $k(\nu,\mathbf{r}')$ are the line shape and the absorption coefficient respectively. Since the PDPs are operated at high pressure ($\sim$500 Torr), pressure broadening originating from collisions between atoms is more dominant than Doppler broadening originating from the Doppler shift due to the thermal motions of the photon-emitting atoms. For the Lorentz line shape by pressure broadening, g and k have the form

$$g(\nu)=\frac{\Delta\nu^L/2\pi}{(\nu-\nu_0)^2+(\Delta\nu^L/2)^2} \quad (5)$$

and

$$k(\nu)=\frac{\lambda_0^2}{8\pi\tau_v}\frac{g_2}{g_1}n_g g(\nu), \quad (6)$$

where λ_0 [=147 nm for $Xe^*(^3P_1)$] and ν_0 [$=2.04\times10^{15}$for $Xe^*(^3P_1)$] are the wavelength and the frequency in the center of the line, g_1 [=1] and g_2 [=3 for $Xe^*(^3P_1)$] are the statistical weights of the ground and excited states, and n_g [n_{Xe} for $Xe^*(^3P_1)$] is the density of the ground-state atom. $\Delta\nu^L$ is the full width at half-maximum of the Lorentz lineshape. From experimental data for Xe–Ne gas mixture,[32] the linewidth is

$$\Delta\nu^L=4.06\times10^{-15}n_{Xe}+1.6\times10^{-16}n_{Ne}, \quad (7)$$

where n_{Xe} and n_{Ne} are the densities of Xe and Ne gases, respectively.

When the ground state density profile is assumed to be uniform, g and k depend only on the frequency of photons. The transmission factor can be simplified and expressed as a function of R:

$$T(\mathbf{r},\mathbf{r}')=T(R)=\int_0^\infty g(\nu)\exp[-k(\nu)R]d\nu. \quad (8)$$

After being integrated using Eqs. (5) and (6), Eq. (8) becomes

$$T(R)=\exp\left(-\frac{k_0R}{2}\right)I_0\left(\frac{k_0R}{2}\right), \quad (9)$$

where $I_0(x)$ is the zeroth-order modified Bessel function and k_0 is defined as

$$k_0 \equiv k(\nu=\nu_0) = \frac{\lambda_0^2}{8\pi\tau_v}\frac{g_2}{g_1}\frac{2}{\pi\Delta\nu^L}n_g, \tag{10}$$

which is the peak absorption coefficient at the line center. For high opacity and low opacity, it can be approximated as

$$T(R) \simeq \begin{cases} (\pi k_0 R)^{-0.5} & \text{for } k_0 R > 0.32 \\ 1 & \text{for } k_0 R < 0.32 \end{cases}. \tag{11}$$

In high opacity limit, the transmission factor is inversely proportional to the square root of the distance, while photons are transparent in low opacity limit. For the Xe*($^3P_1$) resonant atom in the Xe–Ne (4/96%) mixture at pressure of 500 Torr, the critical distance $R_c \equiv 0.32/k_0$ which satisfies $k_0 R = 0.32$ is 0.06 μm. Since the condition $k_0 R > 100$ is satisfied for a typical scale of a PDP cell, the emission from resonant excited states is optically thick.

With a piecewise constant approximation (PCA), the last term in Eq. (1) becomes

$$\int n^*(\mathbf{r}',t)G(\mathbf{r}_k,\mathbf{r}')d\mathbf{r}' = \sum_m^{N_c} n^*(\mathbf{r}_m,t)\int_m G(\mathbf{r}_k,\mathbf{r}')d\mathbf{r}', \tag{12}$$

where $\mathbf{r}_k$ and $\mathbf{r}_m$ are the center positions of the kth and mth cell, respectively. N_c is the number of the simulation cells of the plasma region in three dimensions.

The propagator matrix $A_{k,m}$ is defined as the spatial integral of the kernel function over the volume of the mth cell, which is the probability for a photon emitted within the mth cell to be reabsorbed at the center of kth cell:

$$A_{k,m} \equiv \int_m G(\mathbf{r}_k,\mathbf{r}')d\mathbf{r}' \tag{13}$$

$$= \delta_{k,m} + \int_m \frac{T(R)}{4\pi R^3}\mathbf{R}\cdot\hat{\mathbf{n}}dS. \tag{14}$$

The last equality is derived by using Eq. (3). For convenience, we also define the matrix $A'_{k,m}$:

$$A'_{k,m} \equiv \delta_{k,m} - A_{k,m} \tag{15}$$

$$= -\int_m \frac{T(R)}{4\pi R^3}\mathbf{R}\cdot\hat{\mathbf{n}}dS. \tag{16}$$

Then, the radiation terms in Eq. (1) are simplified by

$$S^r(\mathbf{r}_k,t) + \frac{1}{\tau_v}\int n^*(\mathbf{r}',t)G(\mathbf{r}_k,\mathbf{r}')d\mathbf{r}'$$

$$= S^r(\mathbf{r}_k,t) + \frac{1}{\tau_v}\sum_m^{N_c} A_{k,m}n_m^*(t) \tag{17}$$

$$= -\frac{1}{\tau_v}\sum_m^{N_c} A'_{k,m}n_m^*(t). \tag{18}$$

Using Eq. (11) in high opacity limit, Eq. (16) is represented as three integrals:

$$A'_{k,m} = C_0(A'^{(a)}_{k,m} + A'^{(b)}_{k,m} + A'^{(c)}_{k,m}), \tag{19}$$

where C_0 is $(4\pi\sqrt{\pi k_0})^{-1}$. $A'^{(a)}_{k,m}$, $A'^{(b)}_{k,m}$, and $A'^{(c)}_{k,m}$ are expressed as

$$A'^{(a)}_{k,m} = \int_{x^-_{k,m}}^{x^+_{k,m}}\int_{y^-_{k,m}}^{y^+_{k,m}} dxdy\left[\frac{z^+_{k,m}}{[x^2+y^2+(z^+_{k,m})^2]^{1.75}} - \frac{z^-_{k,m}}{[x^2+y^2+(z^-_{k,m})^2]^{1.75}}\right], \tag{20}$$

$$A'^{(b)}_{k,m} = \int_{x^-_{k,m}}^{x^+_{k,m}}\int_{z^-_{k,m}}^{z^+_{k,m}} dxdz\left[\frac{y^+_{k,m}}{[x^2+z^2+(y^+_{k,m})^2]^{1.75}} - \frac{y^-_{k,m}}{[x^2+z^2+(y^-_{k,m})^2]^{1.75}}\right], \tag{21}$$

and

$$A'^{(c)}_{k,m} = \int_{y^-_{k,m}}^{y^+_{k,m}}\int_{z^-_{k,m}}^{z^+_{k,m}} dydz\left[\frac{x^+_{k,m}}{[y^2+z^2+(x^+_{k,m})^2]^{1.75}} - \frac{x^-_{k,m}}{[y^2+z^2+(x^-_{k,m})^2]^{1.75}}\right], \tag{22}$$

where $x^\pm_{k,m} = x_{k,m} \pm 0.5\Delta x$, $x_{k,m} = |x_k - x_m|$, $y^\pm_{k,m} = y_{k,m} \pm 0.5\Delta y$, $y_{k,m} = |y_k - y_m|$, $z^\pm_{k,m} = z_{k,m} \pm 0.5\Delta z$, and $z_{k,m} = |z_k - z_m|$. $A'^{(a)}_{k,m}$, $A'^{(b)}_{k,m}$, and $A'^{(c)}_{k,m}$ are the integral over the surface segments perpendicular the z-, y-, and x-directions, respectively. In low opacity limit, Eq. (1) becomes the continuity equation by using Eqs. (3) and (11). Thus, the transport of nonresonant species can be accurately described by the continuity equation. The 2D result from Eqs. (19)–(22) can be also obtained in the limit case $\Delta z \to \infty$ and with no integral over the surfaces perpendicular to the z-direction. These results are consistent with those of Ref. 25.

The total photon flux arriving at the position $\mathbf{r}$ on the plane (i.e., phosphor surface) from the plasma region can be obtained by

$$F^{c\to p}(\mathbf{r}) = \int_{V'} \frac{S^r(\mathbf{r}')T(R)}{4\pi R^3}\mathbf{R}\cdot\hat{\mathbf{n}}dV', \tag{23}$$

where V' is the volume of the plasma region and $\hat{\mathbf{n}}$ is the normal vector towards the plane. With the PCA, Eq. (23) can be represented as the photon flux matrix $F_{p,c}$:

$$F^{c\to p}(\mathbf{r}_p) = \sum_c^{N_c} F_{p,c}S^r(\mathbf{r}'_c), \tag{24}$$

where $\mathbf{r}_p$ and $\mathbf{r}_c$ are the center positions of the pth and cth cell, respectively.

We set the plane perpendicular to the y-direction and express $F_{p,c}$ as the sum of two terms:

$$F_{p,c} = F^{(a)}_{p,c} - F^{(b)}_{p,c}. \tag{25}$$

In high opacity limit,

$$F^{(a)}_{p,c} = F^h_0\int_{x^-_{p,c}}^{x^+_{p,c}}\int_{z^-_{p,c}}^{z^+_{p,c}} dxdz[x^2+z^2+(y^-_{p,c})^2]^{-0.75} \tag{26}$$

and

$$F_{p,c}^{(b)}=F_0^h\int_{x_{p,c}^-}^{x_{p,c}^+}\int_{z_{p,c}^-}^{z_{p,c}^+}dxdz[x^2+z^2+(y_{p,c}^+)^2]^{-0.75}, \quad (27)$$

where $F_0^h=(6\pi\sqrt{\pi k_0})^{-1}$. The 2D result from Eqs. (25)–(27) can be also obtained by setting $\Delta z\to\infty$. This result is also consistent with that of Ref. 25. In low opacity limit,

$$F_{p,c}^{(a)}=F_0^l\int_{x_{p,c}^-}^{x_{p,c}^+}\int_{z_{p,c}^-}^{z_{p,c}^+}dxdz[x^2+z^2+(y_{p,c}^-)^2]^{-0.5} \quad (28)$$

and

$$F_{p,c}^{(b)}=F_0^l\int_{x_{p,c}^-}^{x_{p,c}^+}\int_{z_{p,c}^-}^{z_{p,c}^+}dxdz[x^2+z^2+(y_{p,c}^+)^2]^{-0.5}, \quad (29)$$

where $F_0^l=(4\pi)^{-1}$. However, when the plane is on the simulation cell ($x_{p,c}=z_{p,c}=y_{p,c}^l=0$), the expression for $F_{p,c}^{(a)}$ should be changed because the integrand is singular:

$$F_{p,c}^{(a)}=2F_0^l\left[\Delta x\ln\frac{\Delta z+\sqrt{(\Delta x)^2+(\Delta z)^2}}{\Delta x}+\Delta z\ln\frac{\Delta x+\sqrt{(\Delta x)^2+(\Delta z)^2}}{\Delta z}\right] \quad (30)$$

Since nonresonant excited species are in low opacity limit over the whole volume, Eqs. (28)–(30) are used. However, resonant excited species are in low opacity limit or high opacity limit, depending on the distance between the cell and the plane. Since the cell size is usually larger than the critical distance R_c, the expression for $F_{p,c}$ for the case $x_{p,c}=z_{p,c}=y_{p,c}^l=0$ should be the combination of two limits as follows:

$$F_{p,c}^{(a)}=\frac{2-\sqrt{2}}{2}R_c+F_0^h\int_{-0.5\Delta x}^{0.5\Delta x}\int_{-0.5\Delta z}^{0.5\Delta z}dxdz[x^2+z^2+(y_{p,c}^-)^2]^{-0.75}-F_0^h\int_{x^2+z^2<R_c^2,y<R_c}dV[x^2+z^2+(y_{p,c}^-)^2]^{-0.75} \quad (31)$$

and

$$F_{p,c}^{(b)}=F_0^h\int_{-0.5\Delta x}^{0.5\Delta x}\int_{-0.5\Delta z}^{0.5\Delta z}dxdz[x^2+z^2+(y_{p,c}^+)^2]^{-0.75}-F_0^h\int_{x^2+z^2<R_c^2,y<R_c}dV[x^2+z^2+(y_{p,c}^+)^2]^{-0.75}. \quad (32)$$

The first term in Eq. (31) is the result of the integration over cylindrical volume in low opacity limit, while the other terms in Eqs. (31) and (32) are for high opacity limit. Thus, the photon flux of resonant excited species [i.e., $Xe^*(^3P_1)$] is described by Eqs. (26), (27), (31), and (32).

In the PDP cell, some of the emitted UV photons from the plasma discharge reach the phosphor and converted into visible photons. When visible photons are isotropically reemitted and transparent to the gas, the fluxes of visible photons arriving on the output window can be also calculated in a similar way. The nonresonant photon (i.e., visible light) flux arriving at the position $\mathbf{r}$ on the detecting plane (i.e., output window) from the plane (i.e., phosphor surface) emitting photons can be obtained by

$$F^{p\to w}(\mathbf{r})=\int_{S'}\frac{F^{c\to p}(\mathbf{r}')T(R)}{4\pi R^3}\mathbf{R}\cdot\hat{\mathbf{n}}dS', \quad (33)$$

where S' is the area of the emitting plane and $\hat{\mathbf{n}}$ is the normal vector towards the detecting plane. With the PCA,

$$F^{p\to w}(\mathbf{r}_w)=\sum_p^{N_p}F_{w,p}F^{c\to p}(\mathbf{r}_p), \quad (34)$$

where N_p is the number of the simulation cells of the emitting plane.

When both the emitting and detecting planes are perpendicular to the y-direction, the expression of $F_{w,p}$ is as follows:

$$F_{w,p}=(4\pi)^{-1}y_{w,p}\left\{z_{w,p}^+\int_{x_{w,p}^-}^{x_{w,p}^+}dx(x^2+y_{w,p}^2)^{-1}(x^2+y_{w,p}^2+(z_{w,p}^+)^2)^{-0.5}-z_{w,p}^-\int_{x_{w,p}^-}^{x_{w,p}^+}dx(x^2+y_{w,p}^2)^{-1}(x^2+y_{w,p}^2+(z_{w,p}^-)^2)^{-0.5}\right\}. \quad (35)$$

When the emitting and detecting planes are perpendicular to the z-direction and y-direction respectively, the expression of $F_{w,p}$ is

$$F_{w,p}=(4\pi)^{-1}\ln\left(\frac{x_{w,p}^+}{x_{w,p}^-}\frac{+\sqrt{(x_{w,p}^+)^2+(y_{w,p}^-)^2+z_{w,p}^2}}{+\sqrt{(x_{w,p}^-)^2+(y_{w,p}^-)^2+z_{w,p}^2}}\right)-(4\pi)^{-1}\ln\left(\frac{x_{w,p}^+}{x_{w,p}^-}\frac{+\sqrt{(x_{w,p}^+)^2+(y_{w,p}^+)^2+z_{w,p}^2}}{+\sqrt{(x_{w,p}^-)^2+(y_{w,p}^+)^2+z_{w,p}^2}}\right). \quad (36)$$

III. SIMULATION RESULTS

The simulation parameters which we used are as follows. The distance between two sustain electrodes is 60 μm. The neutral gas is a Xe–Ne (4/96%) mixture at pressure of 500 Torr. The secondary electron emission coefficients on the protection layer are 0.5 and 0.05 for neon and xenon ions, respectively. For the $NeXe^+$, the value of 0.5 is used. For the excited species, the same secondary electron emission coefficient with corresponding ions is used. The square pulses with frequency of 100 kHz and voltage of 190 V are applied to two sustain electrodes.

In the TFA, when the the spatial distribution of resonant excited species is assumed to be uniform, the effective decay time is used as the product of the vacuum decay time and the trapping factor:

$$\tau(\mathbf{r})=\tau_v g(\mathbf{r}), \quad (37)$$

The trapping factor can be derived from Eqs. (1) and (3):

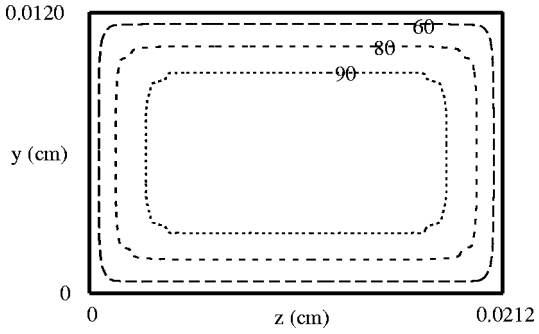

FIG. 1. The spatial profile of the trapping factor in the *yz*-plane calculated from Eq. (38) for Xe 4% fraction. It is shown only in the plasma region. The left and right boundaries are closed by barrier ribs. The upper and bottom boundaries are closed by dielectric materials.

$$g(\mathbf{r})=\left[1-\int G(\mathbf{r},\mathbf{r}')d\mathbf{r}'\right]^{-1}=\left[\int_{S'}\frac{T(R)}{4\pi R^3}\mathbf{R}\cdot\hat{\mathbf{n}}dS'\right]^{-1}, \tag{38}$$

which depends only on the geometry of the system.

Figure 1 shows the spatial profile of the trapping factor in the *yz*-plane for 4% Xe fraction. It is uniform along the *x*-direction because the Neumann boundary condition was applied for the open boundary. The trapping factor is about 1.5 times smaller than that obtained in the two-dimensional simulation in Refs. 22 and 25. The difference comes from one more degree of freedom (i.e., *z*-direction) where the photon can escape.

When the spatial distribution of resonant excited species is identical to the lowest-order eigenmode solution of Holstein equation, the TFA can be also used. When the effective decay time τ is expressed as $\tau_v g_0$, the trapping factor in high opacity limit for Lorentz line in a plane-parallel slab is given by[21]

$$g_0=\frac{\sqrt{\pi k_0 L}}{1.15}, \tag{39}$$

where L is the system length. Because the 2D feature of the PDP cell can be approximated as the slab geometry, this value has been widely used in most of 2D simulations although there is still discrepancy that the spatial distribution of resonant excited species is not the same as obtained in the lowest-order solution. But in three dimensions, the geometry of the PDP cell is also far from the infinite slab. For the same reason as the uniform density case mentioned earlier, the trapping factor in three dimensions should be smaller than the value of Eq. (39) calculated for the slab.

Time evolutions of the total number of Xe*($^3P_1$) and the generation rates of 147-, 150-, and 173-nm UV lights are compared in Fig. 2 for the TFA method and the full RT calculation. For the TFA method, we used Eq. (39) with $L=0.0120$ cm. We can see the discharge with two peaks. The first peak represents the main discharge created by the voltage applied between two sustain electrodes and wall charge generated from the previous discharge. The second one (after 48 μs) is the self-erasing discharge created only by charges accumulated during the main discharge. Here, the main discharge will be focused on rather than the self-erasing one.

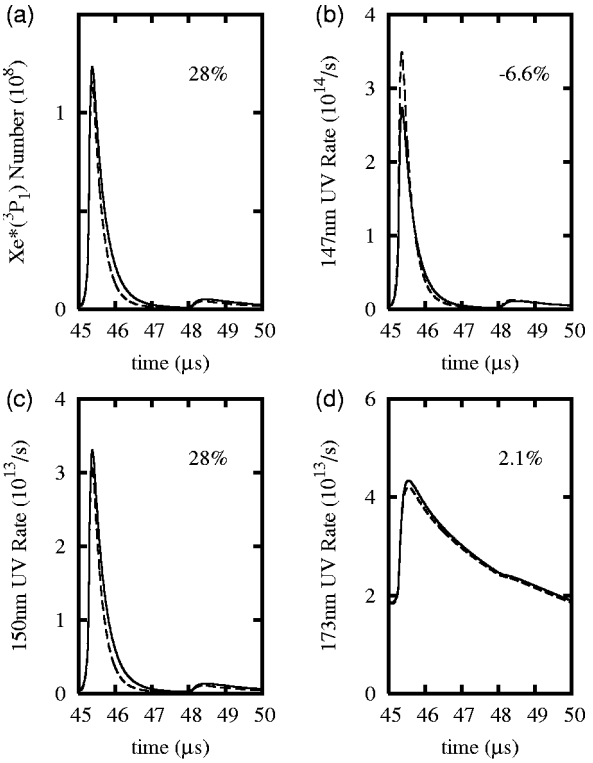

FIG. 2. Time evolutions of (a) the total number of Xe*($^3P_1$) and the generation rates of (b) 147-, (c) 150-, and (d) 173-nm UV lights with the TFA method (solid line) and the full RT calculation (dashed line). The qualitative difference of the time-integrated or time-averaged value of total number over a half-period (from 45 to 50 μs) between two methods is marked in unit of percentage.

Before the number peak of Xe*($^3P_1$), the results of two methods are similar since the production rate due to the electron impact excitation is more dominant than the radiative decay rate. However, in the afterglow, the radiative decay dominates over the production and the discrepancy becomes significant. As shown in Fig. 2(a), the time-averaged value of total number over a half-period (from 45 to 50 μs) in the TFA method is around 28% overestimated compared with the full RT calculation. This discrepancy is larger than 15% of the 2D result of Ref. 25. In the TFA, the trapping factor is constant in time with the assumed profile of the resonant species density. But in the full RT calculation, the effective trapping factor is changed in time as the density profile is changed. As shown in Fig. 2(b), in the beginning the trapping factor in the TFA is overestimated, but in the late afterglow it is underestimated. It is also found that in the TFA, the time-integrated value of the generated 147-nm photons is underestimated. This result is consistent with the overestimation of the total number of the Xe*($^3P_1$) resonant excited state. Due to the related chemical reactions, the overestimation of Xe*($^3P_1$) also leads to the overestimation of total numbers of nonresonant excited species and generation rates of 150- and 173-nm UV light as shown in Figs. 2(c) and 2(d), respectively. Although the generation rate of 150-nm UV is significantly changed, the total amount of UV is not so much affected since the contribution of 150 nm to the total UV is so small when the plasma volume is small.[25]

Figure 3 shows the spatial distributions of Xe*($^3P_1$) cal-

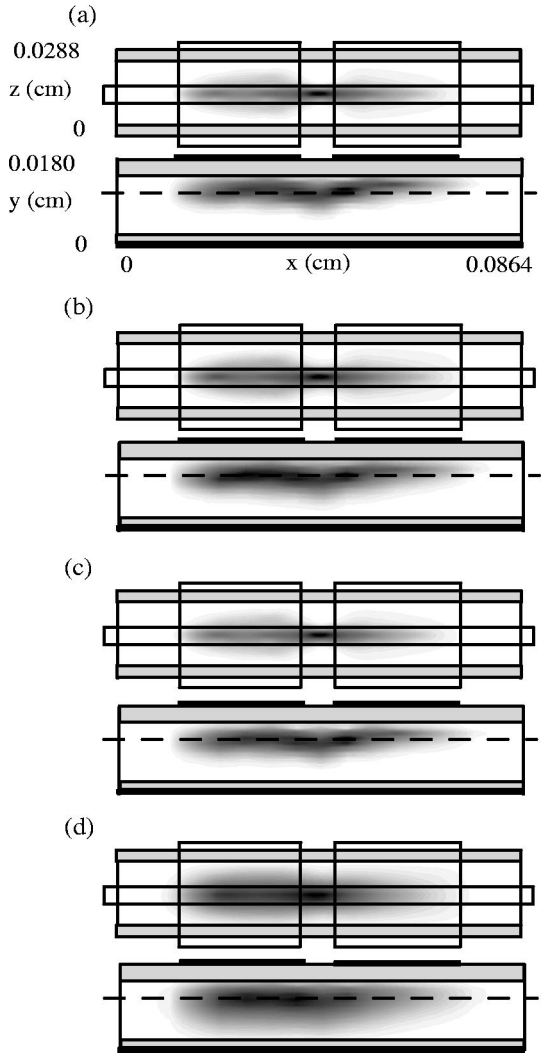

FIG. 3. Comparison of the spatial profiles of the Xe*($^3P_1$) density in *xz*- and *xy*-planes at 45.4 μs [(a) and (b)] and 46.0 μs [(c) and (d)] with the TFA method [(a) and (c)] and the full RT calculation [(b) and (d)]. The left and right electrodes work as the temporal cathode and anode, respectively. The maximum values of each contour are (a) 1.0×10^{12}, (b) 5.2×10^{11}, (c) 3.5×10^{11}, and (d) 2.1×10^{10}cm^{-3}, respectively.

culated with the TFA method [Figs. 3(a) and 3(c)] and the full RT calculation [Figs. 3(b) and 3(d)] at different times. When the redistribution of the density due to the kernel function term [the last term in Eq. (1)] dominates over the production and the redistribution due to the drift-diffusion, it affects the density profile. As shown in Fig. 3(d), the density profile in the late afterglow is broadly distributed compared with the TFA result of Fig. 3(c). The redistributed density profile leads to the change of the effective trapping factor as shown in Fig. 2(b). Our result for the spatiotemporal behavior of the density is similar to the 2D result of Ref. 25.

Using Eqs. (23)–(32), the UV photon fluxes incident upon the bottom and side phosphor layers from the plasma discharge are calculated and the results are presented in Figs. 4(a) and 4(b), respectively. They are time-averaged over the half-period. We assumed that 80% of total UV photons incident upon the phosphor layers are converted into the 496-nm visible photons and visible photons are completely transparent to all the materials. The barrier rib is described in simulation as a rectangular parallelepiped. Using Eqs. (33)–(36), the visible photon flux arriving on the output window from the phosphor layer is calculated [Fig. 4(c)]. There exist two peaks in the distribution of the visible photon flux due to the contribution of the side phosphor layers on the barrier ribs.

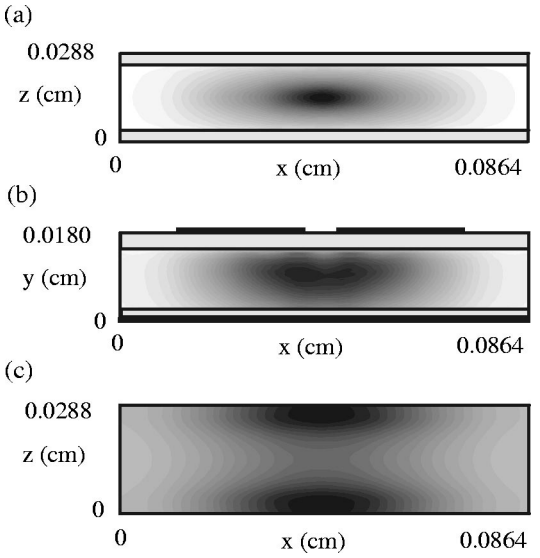

FIG. 4. Distributions of the UV photon flux incident upon (a) the bottom and (b) side phosphor layers from the plasma discharge. (c) Distribution of the visible photon flux arriving at the output window from the phosphor layers. They are time-averaged over the half period. The maximum values of each contour are (a) 2.7×10^{16}, (b) 1.5×10^{16}, and (c) 5.4×10^{15}cm^{-2} s^{-1}, respectively.

Figure 5 shows the schematic diagram of the energy efficiency and the contribution of 147-, 150-, and 173-nm UV lights in unit of percentage from our simulation results. Although 14.7% of the total power consumed in the plasma discharge is used for generating UV photons, only 0.45% of the total power is converted into output visible photons. Thus, the luminous efficiency of the simulated PDP cell is only 1.12 lm/W. The result of the energy efficiency is quantitatively similar to that of Fig. 1 of Ref. 33. The contribution

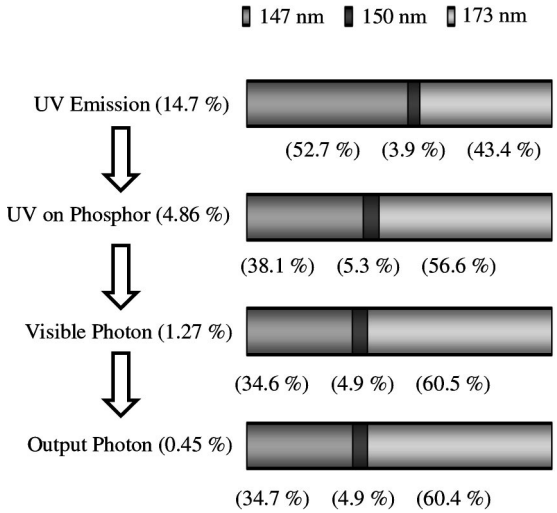

FIG. 5. Schematic diagram of the energy efficiency and the contribution of 147-, 150-, and 173-nm UV lights in unit of percentage from simulations. They are time-averaged over the half-period.

of each UV light is also shown in the diagram. In UV emission, the photon energy of 147-nm light is larger than that of 173-nm light. However, the energy of 147-nm photons arriving on the phosphor layer is smaller than that of 173-nm photons since the discharge is formed nearer to MgO layer side than phosphor side and resonant photons compared with nonresonant ones leave the system through MgO layer side rather than phosphor side. When the TFA is used, the contribution of 147-nm UV light is expected to be underestimated while that of the 150 nm and 173-nm UV lights are expected to be overestimated, as discussed in Fig. 2.

IV. CONCLUSIONS

In order to incorporate the resonance radiation trapping in a PDP cell, we have presented a 3D radiation transport model coupled with a fluid simulation using the propagating function method. Basically, this model is applicable to any fluid simulation which describes the system operated at high pressure where the pressure broadening is the most dominant.

In a PDP cell with xenon and neon mixtures, we compared our results of 3D radiation transport model with those of the conventional trapping factor approach. Analogous to the 2D model of Ref. 25, it showed the differences in the time evolutions of the spatial profile and the total number of the $Xe^*(^3P_1)$ resonant excited state, especially in the afterglow when the radiative decay dominates over the production. The discrepancy of the conventional trapping factor approach came from the pre-assumed density profile and geometry of the PDP cell. Compared with the 2D model, this discrepancy was enhanced due to one more degree of freedom where the photon can escape. The generation rates of 150- and 173-nm UV lights for the two methods were also different due to the related chemical reactions.

We also calculated the visible photon flux reaching the output window from the phosphor layers as well as the total UV photon flux arriving at the phosphor layer from the plasma region for resonant and nonresonant excited states. From these calculations, we obtained the time-averaged spatial distributions of the UV flux on the phosphor layers and the visible photon flux through the output window. Finally, the diagram of the energy efficiency and the contribution of each UV light was shown. It was found that after the generation of UV light the contribution of the resonant excited state to be converted into the visible light becomes small compared with nonresonant one because resonant photons generated from the discharge escape the system mainly through the MgO side which is nearer to their generation position.

Future works are in progress to compare our simulation results with the spatiotemporal profiles of the metastable and resonant states of xenon measured in experiments.

ACKNOWLEDGMENTS

The authors are grateful to Dr. H. J. Lee for the helpful discussion. This work was supported by LG Electronics, Ministry of Education of Korea through its Brain Korea 21 program, and Korea Ministry of Information and Communication under Advanced Backbone IT Technology Development Project.

[1] A. F. Molisch and B. P. Oehry, *Radiation Trapping in Atomic Vapours* (Oxford, New York, 1998).
[2] J. K. Lee and J. P. Verboncoeur, *Plasma Display Panel in Low Temperature Plasma Physics* edited by R. Hippler *et al.* (Wiley-VCH, Berlin, 2001), pp. 367–385.
[3] A. Sobel, IEEE Trans. Plasma Sci. **19**, 1032 (1991).
[4] J. P. Bouef, J. Phys. D **36**, R53 (2003).
[5] K. Tachibana, N. Kosugi, and T. Sakai, Appl. Phys. Lett. **65**, 935 (1994).
[6] K. Tachibana, S. Feng, and T. Sakai, J. Appl. Phys. **88**, 4967 (2000).
[7] K. Tachibana, K. Mizokami, N. Kosugi, and T. Sakai, IEEE Trans. Plasma Sci. **31**, 68 (2003).
[8] J. H. Kim, J. H. Lee, K. W. Whang, and Y. W. Choi, J. Appl. Phys. **89**, 2539 (2001).
[9] Y. Noguchi, A. Matusoka, K. Uchino, and K. Muraoka, J. Appl. Phys. **91**, 613 (2002).
[10] O. Sahni, C. Lanza, and W. E. Howard, J. Appl. Phys. **49**, 2365 (1978).
[11] J. Meunier, P. Belenguer, and J. P. Boeuf, J. Appl. Phys. **78**, 731 (1995).
[12] R. Veerasingam, R. B. Campbell, and R. T. McGrath, Plasma Sources Sci. Technol. **6**, 157 (1997).
[13] C. Punset, J. P. Boeuf, and L. C. Pitchford, J. Appl. Phys. **83**, 1884 (1998).
[14] P. J. Drallos, V. P. Nargony, and W. Williamson, Plasma Sources Sci. Technol. **4**, 576 (1995).
[15] R. B. Campbell, R. Veerasingam, and R. T. McGrath, IEEE Trans. Plasma Sci. **23**, 399 (1995).
[16] H. S. Jeong, Y. Murakami, M. Seki, and H. Murakami, IEEE Trans. Plasma Sci. **29**, 559 (2001).
[17] H. C. Kim, M. S. Hur, S. S. Yang, S. W. Shin, and J. K. Lee, J. Appl. Phys. **91**, 9513 (2002).
[18] W. J. Chung, J. H. Seo, and K. W. Whang, IEEE Trans. Plasma Sci. **30**, 665 (2002).
[19] J. B. Anderson, J. Maya, M. W. Grossman, R. Lagushenko, and J. F. Waymouth, Phys. Rev. A **31**, 2968 (1985).
[20] A. F. Molisch, B. P. Oehry, W. Schupita, and G. Magerl, Comput. Phys. Commun. **93**, 127 (1993).
[21] T. Holstein, Phys. Rev. **72**, 1212 (1947); **83**, 1159 (1951).
[22] G. J. M. Hagelaar, M. H. Klein, R. J. M. M. Snijkers, and G. M. W. Kroesen, J. Appl. Phys. **88**, 5538 (2000).
[23] T. Straaten and M. J. Kushner, J. Appl. Phys. **87**, 2700 (2000).
[24] A. F. Molisch, B. P. Oehry, W. Schupita, and G. Magerl, Comput. Phys. Commun. **93**, 127 (1993).
[25] H. J. Lee, H. C. Kim, S. S. Yang, and J. K. Lee, Phys. Plasmas **9**, 2822 (2002).
[26] J. E. Lawler, G. J. Parker, and W. N. G. Hitchon, J. Quant. Spectrosc. Radiat. Transf. **49**, 627 (1993).
[27] H. J. Lee and J. P. Verboncoeur, Phys. Plasmas **8**, 3077 (2001); **8**, 3089 (2001).
[28] H. J. Lee and J. P. Verboncoeur, J. Appl. Phys. **90**, 4957 (2001).
[29] H. J. Lee and J. P. Verboncoeur, Phys. Plasmas **9**, 4804 (2002).
[30] H. C. Kim, S. S. Yang, and J. K. Lee, IEEE Trans. Plasma Sci. **30**, 188 (2002).
[31] Y. K. Shin, T. S. Hwang, S. D. Kang, H. G. Park, J. H. Ryu, H. C. Kim, S. W. Shin, and J. K. Lee, J. Inf. Dis. **3**, 13 (2002).
[32] K. Igarashi, S. Mikoshiba, Y. Watanabe, M. Suzuki, and S. Murayama, J. Phys. D **28**, 1377 (1995).
[33] R. Ganter, Th. Callegari, L. C. Pitchford, and J. P. Boeuf, Appl. Surf. Sci. **192**, 299 (2002).